

Biochemistry. Author manuscript; available in PMC 2014 September 17.

Published in final edited form as:

Biochemistry. 2013 September 17; 52(37): 6515–6524. doi:10.1021/bi400542z.

Surface reengineering of RPA70N enables co-crystallization with an inhibitor of the RPA interaction motif of ATRIP

Michael D. Feldkamp 1,4 , Andreas O. Frank 1,4,† , J. Phillip Kennedy 3 , James D. Patrone 3 , Bhavatarini Vangamudi 1 , Alex G. Waterson 2,4 , Stephen W. Fesik 1,2,3,4 , and Walter J. Chazin 1,2,4,*

¹Department of Biochemistry, Vanderbilt University, Nashville, TN 37232 (USA)

²Department of Chemistry, Vanderbilt University, Nashville, TN 37232 (USA)

³Department of Pharmacology, Vanderbilt University, Nashville, TN 37232 (USA)

⁴Center for Structural Biology, Vanderbilt University, Nashville, TN 37232 (USA)

Abstract

Replication Protein A (RPA) is the primary single stranded DNA (ssDNA) binding protein in eukaryotes. The N-terminal domain of the RPA70 subunit (RPA70N) interacts via a basic cleft with a wide range of DNA processing proteins, including several that regulate DNA damage response and repair. Small molecule inhibitors that disrupt these protein-protein interactions are therefore of interest as chemical probes of these critical DNA processing pathways and as inhibitors to counter the up-regulation of DNA damage response and repair associated with treatment of cancer patients with radiation or DNA damaging agents. Determination of threedimensional structures of protein-ligand complexes is an important step for elaboration of small molecule inhibitors. However, although crystal structures of free RPA70N and an RPA70Npeptide fusion construct have been reported, RPA70N-inhibitor complexes have been recalcitrant to crystallization. Analysis of the P6₁ lattice of RPA70N crystals led us to hypothesize that the ligand-binding surface was occluded. Surface reengineering to alter key crystal lattice contacts lead to the design of RPA70N E7R, E100R and E7R, E100R mutants. These mutants crystallized in a P2₁2₁2₁ lattice that clearly had significant solvent channels open to the critical basic cleft. Analysis of X-ray crystal structures, target peptide binding affinities, and ¹⁵N-¹H HSQC NMR spectra showed that the mutations do not result in perturbations of the RPA70N ligand-binding surface. The success of the design was demonstrated by determining the structure of RPA70N E7R soaked with a ligand discovered in a previously reported molecular fragment screen. A fluorescence anisotropy competition binding assay revealed this compound can inhibit the interaction of RPA70N with the peptide binding motif from the DNA damage response protein ATRIP. The implications of the results are discussed in the context of ongoing efforts to design RPA70N inhibitors.

Accession numbers

Atomic coordinates and structure factors for the crystal structures of RPA70N E7R, E100R, E7R, E100R, and E7R in complex with VU079104 have been deposited with the Protein Data Bank under accession codes 4IPC, 4IPD, 4IPG, and 4IPH, respectively.

Supporting Information

Supporting material describing the synthesis of VU079104, alternative conformations of select E7R, E100R, and E7R, E100R RPA70N residues, NMR analysis, fluorescence polarization anisotropy assays, and electron density of second molecule of VU079104. This material is available free of charge via the Internet at http://pubs.acs.org.

^{*}To whom correspondence should be addressed, walter.chazin@vanderbilt.edu, Phone: (615) 936-2210.

[†]Present address-Novartis Institutes for BioMedical Research (NIBR), Global Discovery Chemistry, Emeryville, CA USA

Introduction

Replication Protein A (RPA) is the ubiquitous eukaryotic single-stranded (ss) DNA-binding protein that is essential for DNA replication, damage response, repair, and many other DNA transactions(1, 2). RPA functions to protect ssDNA from nucleolytic cleavage as well as prevent reannealing and formation of aberrant DNA structures(3–6). RPA is a heterotrimer of RPA70, RPA32 and RPA14 subunits containing seven folded globular domains and one disordered domain (Figure 1). This modular structure enables it to interact simultaneously with the ssDNA substrate and partner proteins, and thereby serve as a scaffold in a range of DNA processing machines. RPA interacts with other DNA processing proteins via the N, A and B domains from the RPA70 subunit and the C domain from the RPA32 subunit(7). RPA70N has previously been shown to be critical to the interaction of RPA with proteins involved in DNA damage response, including p53, ATRIP, RAD9, and MRE11(8–11). RPA70N binds each of these proteins in a common basic cleft(10).

The DNA damage response (DDR) is required to ensure proper maintenance and propagation of the genome(12, 13). Activation of the Ataxia Telangiectasia and Rad3-related protein (ATR) kinase plays a strategic role in DDR, for example phosphorylating checkpoint protein Chk1 to halt cells in S-phase while DNA repair occurs(10, 14–17). ATR interacting protein (ATRIP) is an obligate co-factor required for stabilizing ATR, which also serves to recruit ATRIP to sites of DNA damage via interactions with RPA(9, 15). An RPA interaction motif near the N-terminus of ATRIP (residues 54–68) has been shown to interact with the basic cleft of RPA70N using NMR spectroscopy(10). This site therefore represents a potential target for development of small molecules that inhibit RPA70N interactions.

A limited set of small molecule RPA70N ligands have already been reported based on high-throughput screens(18–23). However, the interaction of these compounds with RPA is quite weak (K_d in the micromolar range) and the molecular basis for binding has not been defined. Structural information on RPA70N-ligand complexes would greatly enhance the ability to develop inhibitors with substantially higher affinity, which is required for an effective inhibitor in cells. Although RPA70N readily crystallizes and the structure of it and of a fusion of RPA70N to a peptide fragment of p53 have been determined(24), complexes of RPA70N with fragments of other protein targets and of small molecule ligands have yet to be crystallized.

Here we describe the design, production and characterization of RPA70N mutants that crystallize in an alternate lattice. To demonstrate the effectiveness of our approach, one of the mutant proteins is crystallized in complex with a previously identified ligand that competes with the RPA70N interaction motif from ATRIP (25). This first structure of the complex of RPA70N with a small molecule lead inhibitor sets the stage for systematic structure-based design to generate more potent compounds.

Materials and Methods

Site directed mutagenesis, growth and purification of RPA70N mutants

The production of WT RPA70 (1–120) from a pET15b vector (Novagen) was reported previously(25). Primers (Sigma) for preparing the E7R, E100R, and E7R, E100R mutations were used with a Quick-Change Site-Directed Mutagenesis Kit (Stratagene). The mutated plasmids were transformed into BL21-DE3 cells (New England Biolabs) for expression. Growth and purification of unlabeled and ¹⁵N-enriched RPA70N was performed as for the wild-type (WT) protein(10).

Synthesis of VU079104

To a vial containing a solution of methyl 3-isothiocyanatothiophene-2-carboxylate (0.5g, 2.5 mmol, 1 equiv.) in DMF (1 ml) was added a solution of 2-cyano-*N*-(2,3-dimethylphenyl)acetamide (0.47g, 2.5 mmol, 1 equivalent) in DMF (1 ml). To this was added sulfur (0.08g, 2.5 mmol, 1 equivalent) and triethylamine (0.3 ml) and the reaction was heated at 50°C for 1 hour. Once determined complete by LCMS the reaction was allowed to cool to room temperature and poured into a 3% AcOH solution. The solid formed was filtered and washed with methanol to give 0.45g (46% yield) of pure *N*-(2,3-dimethylphenyl)-5-oxo-1-thioxo-4,5-dihydro-1H-thiazolo[3,4-a]thieno[2,3-e]pyrimidine-3-carboxamide (Figure S1) as a yellow solid.

 $^{1}\text{H-NMR}$ (400 MHz, DMSO-d₆): d = 10.11 (br s, 1H), 9.41 (d, J= 5.2 Hz, 1H), 8.30 (d, J= 5.2 Hz, 1H), 7.13 (m, 3H), 2.28 (s, 3H), 2.10 (s, 3H). $^{13}\text{C-NMR}$ (125 MHz, DMSO-d₆): d = 181.0, 160.5, 155.2, 144.7, 141.1, 138.2, 135.5, 133.5, 129.0, 126.4, 125.6, 121.6, 120.7, 21.0, 15.1. High-resolution mass spectroscopy [M + H⁺] calculated for $C_{17}H_{13}N_{3}O_{2}S_{3}$ 388.0248; found: 388.0247.

RPA70N mutant crystallization, data collection and refinement

Crystals of RPA70N E7R, E100R, and E7R, E100R were grown by sitting drop vapor diffusion at 21 °C from a drop composed of equal volumes of protein (7 mg/ml) and reservoir solution. Precipitant solution conditions were: E7R- 100 mM MES (pH 6.5), 200 mM calcium acetate and 20% PEG 8000; E100R- 100 mM BIS-TRIS (pH 5.5), 2 M ammonium sulfate; E7R, E100R- 100 mM citrate (pH 5.0), 200 mM NaCl, 30% PEG 8000. Prior to data collection, crystals were soaked in mother liquor containing 20% 2-methyl-2,4-pentanediol (MPD) and flash frozen in liquid nitrogen. X-ray diffraction data were initially collected on an in-house rotating anode source and later at sector 21 (Life Sciences Collaborative Access Team, LSCAT) at the Advanced Photon Source. All data were processed by HKL2000(26). The proteins crystallized in space group P2₁2₁2₁ and contained one molecule in the asymmetric unit. Initial phases were obtained by molecular replacement with PHASER(26, 27) using the WT- RPA70N structure (2B29) as a search model. Iterative cycles of model building and refinement were performed using COOT and Phenix(28, 29). The structures of RPA70N E7R, E100R, and E7R, E100 have been deposited in the Protein Data Bank under accession codes 4IPC, 4IPD, and 4IPG, respectively.

Crystallization and refinement of the VU079104-E7R RPA70N complex

Crystals of E7R-RPA70N were grown using solution conditions described above. After three days of growth, 1 μ l of 50% PEG 8000 was added the crystal drop and allowed to incubate for 15 minutes, after which 0.5 μ l of 40 mM VU079104 in 100% dimethyl sulfoxide (DMSO) was added for 18 hours. Prior to data collection at LSCAT, MPD was added to a final concentration of 15% and the crystal was flash frozen in liquid nitrogen. Procedures identical to those described above for collection of the E7R structure were performed with the exception that the structure of the mutant was used to obtain initial phase information. Following modeling of waters, VU079104 was placed into electron density at the basic cleft and refined. The structure of this complex has been deposited in the Protein Data Bank under the accession code 4IPH.

Calculation of surface electrostatic charges

Electrostatic surfaces were calculated using the APBS(30) plug-in of Pymol (Scrödinger) using a grid centered upon the center of mass of WT, E7R, E100R, or E7R, E100R. Grid lengths of $74.54 \times 81.5 \times 56$ Å, and $63.8 \times 68 \times 53$ Å were used as coarse and fine grid

calculation inputs respectively. Default APBS settings were used for solvent radius, dielectric, temperature, ionic strength and radius.

NMR Spectroscopy

NMR spectra were acquired using a Bruker AVANCE III 600 MHz spectrometer equipped with a CPQCI cryoprobe. ^{15}N -enriched WT and mutant RPA70N proteins were prepared in a solution containing 50 mM HEPES at pH 7.5 with 100 mM NaCl and 5 mM DTT, while an identical solution supplemented with 5% DMSO was used for VU079104 titrations into WT-RPA70N. Two-dimensional ^{15}N - ^{1}H heteronuclear single quantum coherence (HSQC) spectra were acquired with 128 and 1,024 complex points in the ^{15}N - and ^{1}H -dimension, respectively. Titration experiments were performed using an initial protein concentration of 150 μM with spectra collected at ATRIP54-86 concentrations of 0, 50 100, 200, 385, 740, and 1070 μM or at VU079104 concentrations of 0, 2, 6, 14, 54, 132, 288, 517, and 1034 μM . Data were processed using NMRpipe(31) and analyzed with Sparky (University of California, San Francisco). ^{1}H and ^{15}N backbone NMR assignments for RPA70N were reported previously(10). Chemical shift perturbations were analyzed using a weighted average of the change in chemical shift () upon binding of ATRIP54-68 or VU079104 based on the net perturbations in both the ^{1}H and ^{15}N dimensions calculated using equation (1)(32):

$$\Delta \delta \text{ (ppm)} = [(\Delta^1 H)^2 + (\Delta^{15} N(0.2))^2]^{1/2}$$
 (1)

Fluorescence polarization anisotropy displacement assay

FITC-labeled ATRIP peptide (FITC-Ahx-DFTADDLEELDTLAS-NH₂) amidated at its C-terminus was purchased from NeoBioSci (NEO Group) at >95% HPLC verified purity and reconstituted in DMSO to a final concentration of 1 mM. The peptide equilibrium dissociation constant for binding to WT and RPA70N mutant was determined using a fluorescence polarization anisotropy (FPA) experiment described previously(25). Briefly, increasing concentrations of protein in assay buffer (50 mM HEPES at pH 7.5, 100 mM NaCl, and 5 mM DTT) were incubated with 50 nM FITC-ATRIP in a 96-well flat bottom black well plate (Thermo Fisher Scientific) at room temperature for 1 h. The fluorescence polarization measurements and inhibitor assays were performed using a Wallac 2100 EnVision plate reader (Perkin Elmer). Data were acquired at an excitation wavelength of 480 nm and an emission wavelength of 535 nm. The emission anisotropy values were determined by the Envision software using formulas previously described(25). For peptide or inhibitor binding assays, anisotropy values were plotted against RPA protein or VU079104 concentration and fitted as described previously (25). The dissociation constant (K_d) reported is an average of two independent experiments, each run in duplicate.

RESULTS

Our studies began with co-crystallization trials for RPA70N with small molecules from a high-throughput screen of potential inhibitors (25) using the known conditions for crystallizing the free protein. To drive the equilibrium from the free towards the ligand-bound state, the compounds were added to a concentration > 10-fold higher than their K_d values, i.e. 2 mM of ligand in 250 μ M solutions of RPA70N. Crystals were routinely observed within two days, but no ligand density was observed in any of the 50 different crystals evaluated. Similarly, we were unable to observe density for any ligand from 50 different soaks (5 hours) into preformed WT-RPA70N crystals.

We then systematically analyzed the effect of buffer conditions (pH, ionic strength, additives, and buffering agent) and temperature on the visual appearance of the RPA70N crystals with the goal of finding an alternate crystal morphology. Although all crystals remained in the previously reported hexagonal form(24), we collected datasets for each to determine if any of these crystals exhibited different lattice packing contacts but no differences were observed. We next turned to an analysis of the packing of RPA70N molecules in the hexagonal crystal lattice and observed that the key basic cleft is occluded, which presumably was inhibiting binding to this key interaction surface (Figure 2a-b). We therefore hypothesized that charge reversal mutations of key residues mediating intermolecular contacts would promote crystallization in a lattice better suited to obtaining crystals of the protein-ligand complexes.

E7R, E100R, and E7R, E100R mutations produce crystals in a lattice amenable to soaking

Inspection of the contacts between RPA70N molecules in the crystal revealed that basic cleft residues R31, R41, and R43 contacted E7 and E100 from adjacent molecules (Figure 2a). We therefore created and purified charge-reversal mutants E7R, E100R, and the double mutant E7R, E100R. Standard crystallization trials produced crystals within 72 hours, and inspection under a dissecting light microscope revealed visibly different crystal morphologies than those observed for WT RPA70N. After indexing diffraction data, all three mutants were found to have crystallized in an orthorhombic P2₁2₁2₁ space group. Comparison of the crystal lattices revealed that, unlike the hexagonal crystal lattice observed for WT RPA70N, the basic cleft was exposed to a solvent channel and accessible for binding target peptides and small molecules (Figure 2c). Notably, the P2₁2₁2₁ lattice is the same as that found for the RPA70N-p53 peptide fusion construct with RPA70N arrayed in a similar manner (8).

X-ray crystal structures of E7R, E100R, and E7R, E100R were determined using the molecular replacement approach with WT RPA70N as the search model. The diffraction data were refined to 1.22, 1.51, and 1.58 Å resolution, respectively, i.e. at effectively the same or higher resolution than the 1.60 Å obtained for WT RPA70N. Structural statistics are provided in Table 1. All three mutants adopt the OB-fold structure characterized by a five-stranded -sheet coiled to form a closed -barrel capped by -helices (Figure 3). The data were refined at high resolution, which included modeling of alternative side chain conformations at multiple sites in all three structures.

Evaluation of E7R, E100R and E7R, E100R mutants as models for wild-type RPA70N

The structures of the mutants are all very similar to each other and to WT RPA70N. The pairwise C RMSD values between the mutants are 0.27 Å (E7R vs E100R), 0.20 Å (E7R vs E7, E100R), and 0.22 Å (E100R vs E7R, E100R). Superposition of the mutants with WT RPA70N for E7R, E100R and E7R, E100R produced all C atom RMSDs of 0.45, 0.43, and 0.42 Å, respectively (Figure 3). Slight shifts of flexible loop residues located between sheets 1-2 and 4-5 were also noted when comparing the structures to WT RPA70N. These shifts are attributed to the new crystal lattice contacts made in the orthorhombic crystal lattice as they involve a different set of residue contacts than those used by the loops in the WT RPA70N hexagonal crystal lattice. A number of new crystal contacts formed by the charge reversal mutations were also noted. In the case of E7R, R7 contacts (3.5 Å or less) T34, N85, and K88 of symmetry related molecules. In E100R, R100 contacts Q15, S73, N74, G109, E120 of symmetry related molecules. Similarly, in the E7R, E100R mutant, R7 contacts T34, N85, and K88 and R100 contacts S73, N74, G109 and E120 of symmetry related molecules. Closer inspection revealed that even the most statistically significant differences are relatively modest; these occur primarily for solvent-exposed side chains that change rotamers, including R41, R43, and R91 (Figure S2).

The structures of the RPA70N mutants were further assessed by calculating electrostatic surface potentials (Figure 4). Importantly, the key basic ligand-binding clefts of the mutants are indistinguishable from WT RPA70N. Thus, as anticipated, charge reversal of E7 and E100 resulted in substantial changes in the electrostatic potential in the vicinity of the mutation sites. However, since these are at the opposite side of the molecule, these mutations did not significantly alter the critical basic ligand-binding surface of RPA70N.

To further validate the three mutants as suitable models for WT RPA70N, their interactions with the RPA interaction motif from the N-terminal region of the DDR kinase ATR/ATRIP were investigated. Following our previously reported study(25), ¹⁵N-¹H HSQC NMR spectroscopy was used to determine the residues in the mutant proteins that were affected upon binding of ATRIP₅₄₋₆₈ (Figure 5A, S3). The NMR chemical shift perturbations observed were nearly identical in all three mutant proteins and corresponded well to those observed in a corresponding titration of WT RPA70N. Indeed, the magnitude of chemical shift perturbations calculated in terms of global chemical shift correlation is similar (Figure 5B). The slope of these plots provides correlations to WT of 1.01, 1.04, and 1.01 for E7R, E100, and E7R, E100R, respectively, indicating a very high degree of structural similarity among the complexes with ATRIP₅₄₋₆₈.

Our previously developed fluorescence polarization anisotropy (FPA) assay was then used to measure the binding affinity of ATRIP₅₄₋₆₈ for WT, E7R, E100R, and E7R, E100R (Figure S4)(25). Binding curves were generated by fitting anisotropy values to a single-site binding model and yielded binding affinities that were very similar to each other (Table 2). These data confirmed that the charge reversal mutations designed to alter the crystal packing do not alter the target binding properties of RPA70N.

Overall, these analyses show that the structures of the mutants are very similar to the WT protein and in particular that the key ligand-binding site is not perturbed. Hence, reengineering of the surface charge to disrupt the hexagonal crystal lattice was successful and generated the desired model for co-crystallization of WT RPA70N with target peptides and small molecule ligands.

Structure of a VU079104-E7R complex

To demonstrate that co-crystal structures could be obtained, we co-crystallized E7R with VU079104 from our previously reported molecular fragment screen(25) and determined the X-ray crystal structure (Figure 6a). Since the affinity of small molecules for RPA70N is typically in the micromolar range, our crystallization strategy involved soaking preformed crystals of E7R in a solution containing 10 mM ligand to promote saturation of all protein molecules. The E7R mutant was selected for this experiment because it produced the largest crystals among the three mutants. The crystals were soaked for 18 hours after which they were harvested and flash frozen in liquid nitrogen and screened for diffraction. Full data sets were collected for all such crystals and after initial refinement of the best diffracting crystal, electron density was clearly evident in the basic cleft (Figure 6b). The density was readily fit with the VU079104 ligand, and after optimization, the structure was refined to a final resolution of 1.94 Å (Table 1).

The backbone of E7R did not change significantly upon ligand binding, but multiple side chain rearrangements did occur to accommodate VU079104 within the basic cleft. Two molecules of the VU079104 were identified per molecule of E7R within the asymmetric unit. One ligand molecule makes numerous intermolecular contacts within the basic cleft (Figure 6b), including notable hydrophobic contacts with I33, V93, and I95, as well as two direct hydrogen bonds to R41 and N85. The positions of the latter two residues are shifted upon binding of the ligand with the side chain of R41 moving by 0.9 Å and that of N85

shifting from multiple side chain conformations to occupying a single rotamer (Figure 6c). In contrast, the second VU079104 molecule had no significant contact with the protein.

The second molecule only became apparent after placement of the first VU079104 molecule into the F_o - F_c electron density map. Additional F_o - F_c electron density was observed that corresponded well to another VU079104 molecule. This second molecule makes hydrophobic pi stacking interactions with the first molecule of VU79104 in a slightly offset orientation, which presumably maximizes the favorable aromatic stacking interactions (Figure S5). The second VU079104 molecule is likely an artifact of crystallization, and is possible because the solvent channel within the orthorhombic crystal lattice is quite large. The only interaction with the protein is one weak contact to the side chain -nitrogen of R41 at 3.4 Å.

VU079104 interacts with the basic cleft of RPA70N in solution

Although the structure of E7R-VU079104 complex shows the ligand bound in the basic cleft, it is important to confirm that this is the actual binding site in solution. Consequently, a $^{15}N^{-1}H$ HSQC NMR titration was used to map residues whose chemical environment was perturbed upon binding of VU079104 (Figure 7a). The observation of RPA70N chemical shift perturbations within the fast exchange limit over the course of the titration is consistent with binding of the ligand in the μ M regime. Mapping of the chemical shift perturbations onto the crystal structure of E7R in the VU079104 complex (Figure 7b and 7c), shows the expected binding in the basic cleft. This data indicates that the binding site for VU079104 is the same in the crystal and solution, demonstrating that soaking into preformed crystals does not mask conformational changes required for binding.

VU079104 inhibits binding of ATRIP interaction motif

To investigate if VU079104 is capable of inhibiting protein-protein interactions, our previously described fluorescence anisotropy assay was performed (25). This competition based assay uses a FITC-labeled ATRIP54-68 peptide, which was shown to undergo a large change in fluorescence anisotropy upon binding to RPA70N and a return to the starting state when another molecule is able to displace the peptide from the protein. Figure 8 shows the displacement curve obtained when VU079104 is titrated into the solution of the RPA70N-peptide complex. Fitting of these data to a standard single-site binding equation provides a K_d of $41.4 \pm 3.2~\mu M$. These data show VU079104 is capable of displacing the peptide from the basic cleft of RPA70N. This result, combined with the crystal structure of the complex and our NMR analyses, indicates that VU079104 represents a viable initial lead compound for development of an RPA70N inhibitor.

Structure-based leads for elaboration of VU079104

Previous studies from our laboratory have established a common set of residues within the RPA70N basic cleft that are used for binding ATRIP, Rad9, and MRE11(10). Our structure of the RPA70N-VU079104 complex shows that this ligand binds directly in the basic cleft and orients itself by hydrogen bonding with R41 and N85. Notably, many of the same hydrophobic contacts utilized to bind VU079104 are also made in the complex with the p53 peptide(24). This suggests VU079104 is a viable scaffold upon which chemical modifications can be introduced to produce a more potent RPA70N inhibitor.

Comparison of RPA70N binding interface residues located within 4 Å of VU079104 to those utilized in the binding of the p53 peptide (Figure 6d) reveals solvent exposed surfaces surrounding VU079104 that can be utilized to produce analogs of increased affinity. Using the contact surface of p53 in the basic cleft of RPA70N as a guide, possible routes for elaboration of the molecule can be envisioned. It is well known that RPA70N interaction

motifs are acidic (10). In this vein VU079104 can be extended with carboxylate functional groups directed toward the basic residues R41 and/or R81. Incorporation of this favorable charge-charge interaction into the three membered ring system will likely offer a reasonable boost in affinity. A more significant gain in affinity may be realized through occupation of the hydrophobic pocket centered on S55 (Figure 6d). Addition of a phenyl group to the 2,3-dimethylphenyl ring of VU079104 via a linker of appropriate length would mimic the structure of the RPA70N-p53₄₄₋₅₈ fusion protein, as F54 makes hydrophobic contacts in this pocket (Figure 9) and buries 74.9 Å² of solvent exposed hydrophobic surface. Additional potential salt bridge interactions or hydrogen bonds with nearby RPA70N residues R43 and R91 represent attractive additional stabilizing interactions since these residues have been shown previously to play important roles in target binding(10) (Figure 9).

Discussion

Small molecule discovery is greatly aided by the availability of high-resolution structures of protein-ligand complexes(33). The pursuit of such an approach is highly relevant for efforts to identify effective inhibitors of RPA70N, as direct high-throughput screens have yet to turn up compounds with affinities in the desired nM range. It is well known that crystal packing can inhibit the binding of ligands when the critical protein surfaces are rendered inaccessible by lattice contacts, as is seen here for crystals of WT RPA70N. Alternate crystal morphologies can be produced sometimes by changing the solution used for crystallization. However, screening of over 500 sparse matrix crystallization conditions for RPA70N did not produce any alternate crystal forms. An alternate crystal morphology was produced in the previously reported structure of a RPA70N-p53 fusion construct(24). However, covalent linkage of VU079104 and other fragment lead molecules is not routinely feasible and would likely bias the resulting structure.

Approaches for disrupting the crystal packing contacts that favor an unwanted crystal form include reengineering residues at the protein surface or fusing the protein of interest to a known highly crystallizable protein (reviewed in (34-37)). Fusion of RPA70N to maltose binding protein or lysozyme was not applied here because tethering may have blocked the ligand binding surface. Aside from the protein fusion strategy, the other strategies are based on targeting solvent exposed surface residues, which are the mediators of crystal lattice contact points. Mutation of Arg and Lys residues to reduce surface entropy is a common approach(39). This was not chosen for our system because the most obvious crystal contacts in the lattice of the wild type protein are from Arg and Lys residues in the critical basic cleft of RPA70N where our inhibitors need to bind. Recently, systematic mutagenesis of surface residues and/or deletion of loops and disordered regions has been used to produced a significantly higher resolution resolution structure for a complex of the HIV reverse transcriptase and a small molecule inhibitor TMC278(38). Although this highly systematic approach was successful, in reference to RPA70N, care would be needed to avoid perturbing the critical basic cleft. Moreover, this study required the generation, expression and crystallization of > 60 different protein constructs.

The approaches noted above do not require knowledge of the three dimensional structure of the protein of interest and have proven to be relatively robust. However, when the structure is available, it is possible to examine the specific crystal lattice contacts and design modifications to the surface residues involved in a highly targeted and efficient manner. Inspection of the structure of WT RPA70N revealed that in its $P6_1$ lattice, the key residues in the basic cleft mediate crystal lattice contacts, interacting with acidic residues on the opposite face of another RPA70N molecule. We therefore designed charge reversal mutation of the acidic residues E7 and E100, which are distant from the basic cleft, and found that these are sufficient to achieve the goal of producing the change in crystal lattice packing

with minimal alteration of RPA70N. A similar approach employing charge neutralization of surface glutamate residues has been reported in a recent study of the Kelch domain of human Keap1 (40). We note that in contrast to a number of other surface re-engineering studies in which more than one surface mutation or tethering to another protein was required to induce alternate crystal lattice packing(38, 41–43), a single point mutation at E7 or E100 was sufficient to generate the new crystal packing lattice for RPA70N.

The effects of a mutation on the physical properties of a protein should always be investigated to ensure that the mutant represents an accurate model for the wild type protein. WT RPA70N carries a net charge of zero with a pI of 6.93, whereas the charge reversal mutants have relative net charges of +1 (E7R or E100R) or +2 (E7R, E100R) with pI values of 8.73 and 9.44, respectively. No significant perturbations were observed in the high-resolution crystal structures of either mutants. Increasing the net positive charge of RPA70N could conceivably affect long-range electrostatic interactions, particularly as all known RPA70N ligands have an electrostatic component to binding. However, we note that no significant differences with respect to WT protein were observed in the binding affinities of the mutants for the highly acidic ATRIP peptide (net charge of –6). This observation is consistent with the electrostatic field potentials calculated at the ligand-binding surface, which predict no differences in electrostatic field in the basic cleft between the mutants and WT protein (Figure 4).

The increase in resolution obtained for E7R correlates with a more ordered and stable crystalline lattice. This added stability of the lattice provides an extra benefit for the soaking of small organic molecules such as VU079104, which are commonly dissolved in DMSO. This extra stability of the lattice proved valuable in this case as 25% DMSO is required for generating a saturated solution of VU079104. Hence, initial attempts to soak the ligand into WT RPA70N crystals led to dissolution of the crystal. In contrast, the more stable crystal lattice attained for E7R is more tolerant of DMSO and affords the opportunity to determine the structures of complexes with other ligands having limited aqueous solubility.

Conclusions

The studies described here establish for the first time a structural basis for inhibition of the basic cleft of RPA70N. We showed that VU079104 is capable of displacing a peptide derived from the DNA damage response protein ATRIP. In addition, the results presented here validate the use of RPA70N charge reversal mutants E7R, E100R, and E7R, E100R as suitable artifact-free crystallization platforms that can be used in future structure-based inhibitor design efforts.

DNA damage response and repair are up-regulated in response to radiation and chemotherapy treatments, which elicit their effect by damaging DNA. Since accumulation of RPA-coated ssDNA is a signal for the initiation of the DNA damage response, RPA70N inhibitors that block interactions with key partner proteins could disrupt the mobilization of the DNA damage response proteins and restart of stalled replication forks. RPA70N inhibitors that suppress the DNA damage response and subsequent repair therefore have the potential to sensitize cancer cells to the DNA damaging agents that are currently being used to treat cancer patients. Thus, the RPA70N mutants presented here are of considerable value to ongoing structure-based discovery efforts targeted to generating RPA70N inhibitors with therapeutic potential for the treatment of cancer.

Supplementary Material

Refer to Web version on PubMed Central for supplementary material.

Acknowledgments

We would like to thank Dr. David Cortez for his intellectual contributions in the conception of this project, Dr. Olivia Rossanese for the critical reading of the manuscript, and the Life Sciences Collaborative Access Team (LS-CAT) staff at the Advanced Photon Source for help with data collection. Use of the Advanced Photon Source, an Office of Science User Facility operated for the U.S. Department of Energy (DOE) Office of Science by Argonne National Laboratory, was supported by the U.S. DOE under Contract No. DE-AC02-06CH11357. Use of the LS-CAT Sector 21 was supported by the Michigan Economic Development Corporation and the Michigan Technology Tri-Corridor (Grant 085P1000817).

This research was supported in part by grants from the National Institutes of Health: R01 GM65484 and P01 CA092584 to W.J.C., DP1 OD006933/DP1 CA174419 to S.W.F., RC2CA148375 to L.J. Marnett, P30 ES00267 to the Vanderbilt Center in Molecular Toxicology, and P30 CA068485 to the Vanderbilt Ingram Cancer Center. MDF was supported by NIH NRSA postdoctoral fellowship F32 ES021690, AOF by a postdoctoral fellowship from the German Academic Exchange Service Deutscher Akademischer Austausch Dienst and JP by NIH NRSA postdoctoral fellowship F32 CA174315.

References

- 1. Wold MS, Kelly T. Purification and characterization of replication protein A, a cellular protein required for in vitro replication of simian virus 40 DNA. Proc Natl Acad Sci U S A. 1988; 85:2523–2527. [PubMed: 2833742]
- 2. Wold MS. Replication protein A: a heterotrimeric, single-stranded DNA-binding protein required for eukaryotic DNA metabolism. Annu Rev Biochem. 1997; 66:61–92. [PubMed: 9242902]
- Bochkarev A, Pfuetzner RA, Edwards AM, Frappier L. Structure of the single-stranded-DNAbinding domain of replication protein A bound to DNA. Nature. 1997; 385:176–181. [PubMed: 8990123]
- Lao Y, Gomes XV, Ren Y, Taylor JS, Wold MS. Replication protein A interactions with DNA. III. Molecular basis of recognition of damaged DNA. Biochemistry. 2000; 39:850–859. [PubMed: 10653628]
- 5. Treuner K, Ramsperger U, Knippers R. Replication protein A induces the unwinding of long double-stranded DNA regions. J Mol Biol. 1996; 259:104–112. [PubMed: 8648638]
- 6. Zou L, Liu D, Elledge SJ. Replication protein A-mediated recruitment and activation of Rad17 complexes. Proc Natl Acad Sci U S A. 2003; 100:13827–13832. [PubMed: 14605214]
- 7. Fanning E, Klimovich V, Nager AR. A dynamic model for replication protein A (RPA) function in DNA processing pathways. Nucleic Acids Res. 2006; 34:4126–4137. [PubMed: 16935876]
- 8. Dutta A, Ruppert JM, Aster JC, Winchester E. Inhibition of DNA replication factor RPA by p53. Nature. 1993; 365:79–82. [PubMed: 8361542]
- 9. Cortez D, Guntuku S, Qin J, Elledge SJ. ATR and ATRIP: partners in checkpoint signaling. Science. 2001; 294:1713–1716. [PubMed: 11721054]
- Xu X, Vaithiyalingam S, Glick GG, Mordes DA, Chazin WJ, Cortez D. The basic cleft of RPA70N binds multiple checkpoint proteins, including RAD9, to regulate ATR signaling. Mol Cell Biol. 2008; 28:7345–7353. [PubMed: 18936170]
- 11. Lee SE, Moore JK, Holmes A, Umezu K, Kolodner RD, Haber JE. Saccharomyces Ku70, mre11/rad50 and RPA proteins regulate adaptation to G2/M arrest after DNA damage. Cell. 1998; 94:399–409. [PubMed: 9708741]
- 12. Nam EA, Cortez D. ATR signalling: more than meeting at the fork. Biochem J. 2011; 436:527–536. [PubMed: 21615334]
- Bensimon A, Aebersold R, Shiloh Y. Beyond ATM: the protein kinase landscape of the DNA damage response. FEBS Lett. 2011; 585:1625–1639. [PubMed: 21570395]
- 14. Namiki Y, Zou L. ATRIP associates with replication protein A-coated ssDNA through multiple interactions. Proc Natl Acad Sci U S A. 2006; 103:580–585. [PubMed: 16407120]
- 15. Ball HL, Ehrhardt MR, Mordes DA, Glick GG, Chazin WJ, Cortez D. Function of a conserved checkpoint recruitment domain in ATRIP proteins. Mol Cell Biol. 2007; 27:3367–3377. [PubMed: 17339343]

16. Ball HL, Myers JS, Cortez D. ATRIP binding to replication protein A single-stranded DNA promotes ATR-ATRIP localization but is dispensable for Chk1 phosphorylation. Mol Biol Cell. 2005; 16:2372–2381. [PubMed: 15743907]

- Olson E, Nievera CJ, Klimovich V, Fanning E, Wu X. RPA2 is a direct downstream target for ATR to regulate the S-phase checkpoint. J Biol Chem. 2006; 281:39517–39533. [PubMed: 17035231]
- Anciano Granadillo VJ, Earley JN, Shuck SC, Georgiadis MM, Fitch RW, Turchi JJ. Targeting the OB-Folds of Replication Protein A with Small Molecules. J Nucleic Acids. 2010; 2010:304035.
 [PubMed: 21188165]
- Shuck SC, Turchi JJ. Targeted inhibition of Replication Protein A reveals cytotoxic activity, synergy with chemotherapeutic DNA-damaging agents, and insight into cellular function. Cancer Res. 2010; 70:3189–3198. [PubMed: 20395205]
- 20. Andrews BJ, Turchi JJ. Development of a high-throughput screen for inhibitors of replication protein A and its role in nucleotide excision repair. Mol Cancer Ther. 2004; 3:385–391. [PubMed: 15078981]
- 21. Glanzer JG, Liu S, Oakley GG. Small molecule inhibitor of the RPA70 N-terminal protein interaction domain discovered using in silico and in vitro methods. Bioorg Med Chem. 2011; 19:2589–2595. [PubMed: 21459001]
- 22. Shuker SB, Hajduk PJ, Meadows RP, Fesik SW. Discovering high-affinity ligands for proteins: SAR by NMR. Science. 1996; 274:1531–1534. [PubMed: 8929414]
- 23. Petros AM, Huth JR, Oost T, Park CM, Ding H, Wang X, Zhang H, Nimmer P, Mendoza R, Sun C, Mack J, Walter K, Dorwin S, Gramling E, Ladror U, Rosenberg SH, Elmore SW, Fesik SW, Hajduk PJ. Discovery of a potent and selective Bcl-2 inhibitor using SAR by NMR. Bioorg Med Chem Lett. 2010; 20:6587–6591. [PubMed: 20870405]
- 24. Bochkareva E, Kaustov L, Ayed A, Yi GS, Lu Y, Pineda-Lucena A, Liao JC, Okorokov AL, Milner J, Arrowsmith CH, Bochkarev A. Single-stranded DNA mimicry in the p53 transactivation domain interaction with replication protein A. Proc Natl Acad Sci U S A. 2005; 102:15412–15417. [PubMed: 16234232]
- 25. Souza-Fagundes EM, Frank AO, Feldkamp MD, Dorset DC, Chazin WJ, Rossanese OW, Olejniczak ET, Fesik SW. A high-throughput fluorescence polarization anisotropy assay for the 70N domain of replication protein A. Anal Biochem. 2011
- 26. Otwinowski Z, Minor W. Processing of X-ray Diffraction Data Collected in Oscillation Mode. Methods in Enzymology. 1997; 276:307–326.
- 27. Winn MD, Ballard CC, Cowtan KD, Dodson EJ, Emsley P, Evans PR, Keegan RM, Krissinel EB, Leslie AG, McCoy A, McNicholas SJ, Murshudov GN, Pannu NS, Potterton EA, Powell HR, Read RJ, Vagin A, Wilson KS. Overview of the CCP4 suite and current developments. Acta Crystallogr D Biol Crystallogr. 2011; 67:235–242. [PubMed: 21460441]
- 28. Emsley P, Cowtan K. Coot: model-building tools for molecular graphics. Acta Crystallogr D Biol Crystallogr. 2004; 60:2126–2132. [PubMed: 15572765]
- Adams PD, Afonine PV, Bunkoczi G, Chen VB, Davis IW, Echols N, Headd JJ, Hung LW, Kapral GJ, Grosse-Kunstleve RW, McCoy AJ, Moriarty NW, Oeffner R, Read RJ, Richardson DC, Richardson JS, Terwilliger TC, Zwart PH. PHENIX: a comprehensive Python-based system for macromolecular structure solution. Acta Crystallogr D Biol Crystallogr. 2010; 66:213–221. [PubMed: 20124702]
- 30. Baker NA, Sept D, Joseph S, Holst MJ, McCammon JA. Electrostatics of nanosystems: application to microtubules and the ribosome. Proc Natl Acad Sci U S A. 2001; 98:10037–10041. [PubMed: 11517324]
- 31. Delaglio F, Grzesiek S, Vuister GW, Zhu G, Pfeifer J, Bax A. NMRPipe: a multidimensional spectral processing system based on UNIX pipes. J Biomol NMR. 1995; 6:277–293. [PubMed: 8520220]
- 32. Hoffman RM, Li MX, Sykes BD. The binding of W7, an inhibitor of striated muscle contraction, to cardiac troponin C. Biochemistry. 2005; 44:15750–15759. [PubMed: 16313178]
- 33. Muchmore SW, Hajduk PJ. Crystallography, NMR and virtual screening: integrated tools for drug discovery. Curr Opin Drug Discov Devel. 2003; 6:544–549.

34. Ruggiero A, Smaldone G, Squeglia F, Berisio R. Enhanced crystallizability by protein engineering approaches: a general overview. Protein Pept Lett. 2012; 19:732–742. [PubMed: 22489782]

- 35. Derewenda ZS. It's all in the crystals. Acta Crystallogr D Biol Crystallogr. 2011; 67:243–248. [PubMed: 21460442]
- 36. Bolanos-Garcia VM, Chayen NE. New directions in conventional methods of protein crystallization. Prog Biophys Mol Biol. 2009; 101:3–12. [PubMed: 20018205]
- 37. Dale GE, Oefner C, D'Arcy A. The protein as a variable in protein crystallization. J Struct Biol. 2003; 142:88–97. [PubMed: 12718922]
- 38. Bauman JD, Das K, Ho WC, Baweja M, Himmel DM, Clark AD Jr, Oren DA, Boyer PL, Hughes SH, Shatkin AJ, Arnold E. Crystal engineering of HIV-1 reverse transcriptase for structure-based drug design. Nucleic Acids Res. 2008; 36:5083–5092. [PubMed: 18676450]
- 39. Goldschmidt L, Cooper DR, Derewenda ZS, Eisenberg D. Toward rational protein crystallization: A Web server for the design of crystallizable protein variants. Protein Sci. 2007; 16:1569–1576. [PubMed: 17656576]
- 40. Horer S, Reinert D, Ostmann K, Hoevels Y, Nar H. Crystal-contact engineering to obtain a crystal form of the Kelch domain of human Keap1 suitable for ligand-soaking experiments. Acta Crystallogr Sect F Struct Biol Cryst Commun. 2013; 69:592–596.
- 41. Moon AF, Mueller GA, Zhong X, Pedersen LC. A synergistic approach to protein crystallization: combination of a fixed-arm carrier with surface entropy reduction. Protein Sci. 2010; 19:901–913. [PubMed: 20196072]
- 42. Yamada H, Tamada T, Kosaka M, Miyata K, Fujiki S, Tano M, Moriya M, Yamanishi M, Honjo E, Tada H, Ino T, Yamaguchi H, Futami J, Seno M, Nomoto T, Hirata T, Yoshimura M, Kuroki R. 'Crystal lattice engineering,' an approach to engineer protein crystal contacts by creating intermolecular symmetry: crystallization and structure determination of a mutant human RNase 1 with a hydrophobic interface of leucines. Protein Sci. 2007; 16:1389–1397. [PubMed: 17586772]
- 43. Derewenda ZS. Rational protein crystallization by mutational surface engineering. Structure. 2004; 12:529–535. [PubMed: 15062076]

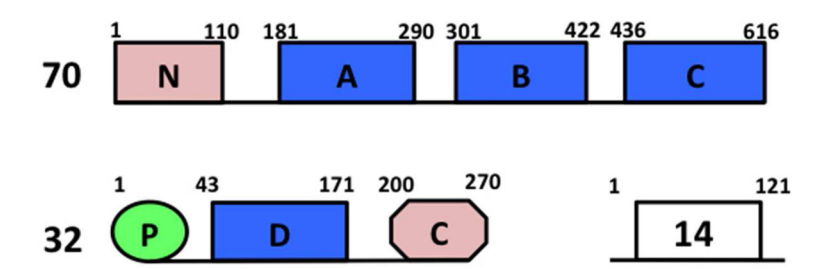


Figure 1. Subunit and domain structure of RPA

OB-fold domains are depicted as rectangles, the winged helix-turn-helix domain as an octagon and the unstructured phosphorylation domain as an oval. The ssDNA binding domains are RPA70A 70B, 70C and 32D (blue). Domains RPA70N and RPA32C are the primary protein recruitment modules (pink). The RPA trimer is formed by interactions between RPA70C, RPA32D, and RPA14.

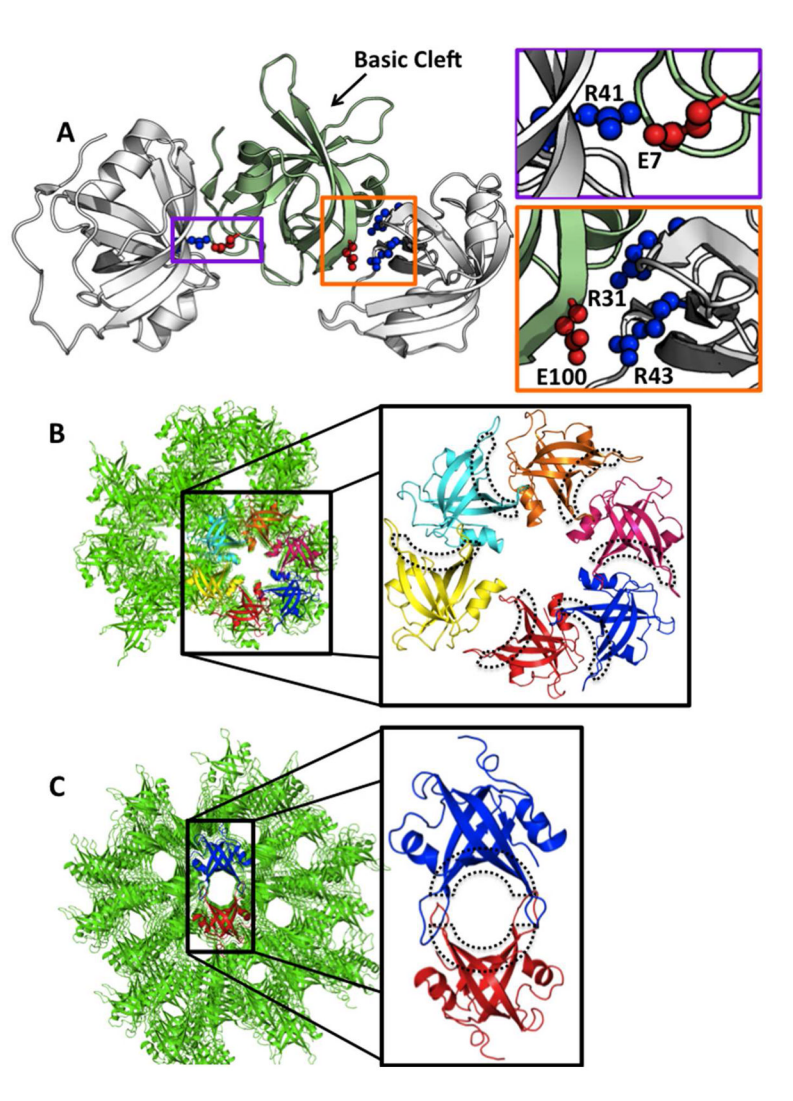


Figure 2. Packing of RPA70N in hexagonal and orthorhombic crystal lattices

A) Lattice contacts in the hexagonal crystal lattice between residues E7 and E100 (red) and basic cleft residues R31, R41, and R43 (blue) from an adjacent RPA70N molecule. B) Packing of the basic cleft of RPA70N against the backside of its symmetry mate in the hexagonal crystal lattice blocks access to the basic cleft (dashed line). C) Packing in the orthorhombic lattice adopted by RPA70N charge reversal mutants produces solvent channels formed directly by the basic clefts (dashed line) of opposing RPA70N symmetry mates.

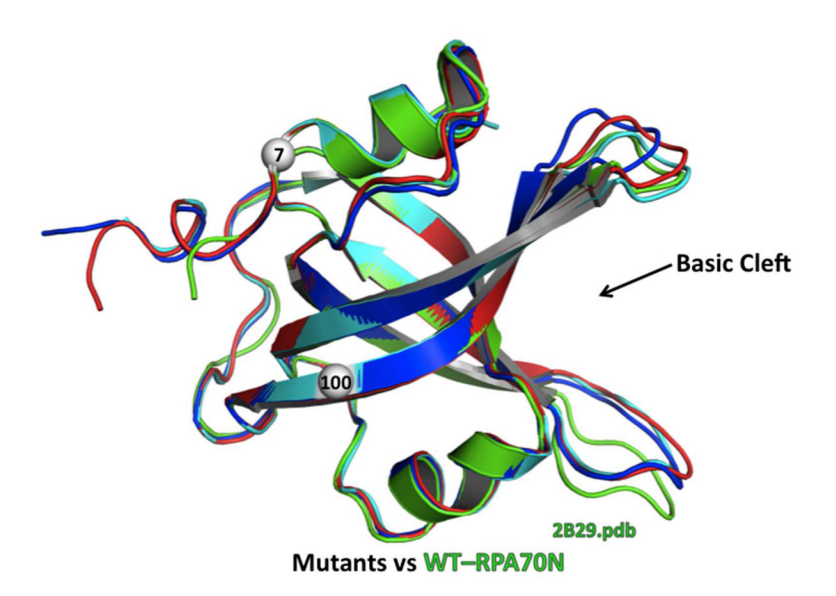


Figure 3. Comparison of the structures of WT RPA70N and the E7R, E100R, and E7R, E100R mutants

A) Best-fit superposition (C atoms) of the structures of E7R (red), E100R (blue), and E7R-E100R (cyan) on the structure of WT RPA70N (green).

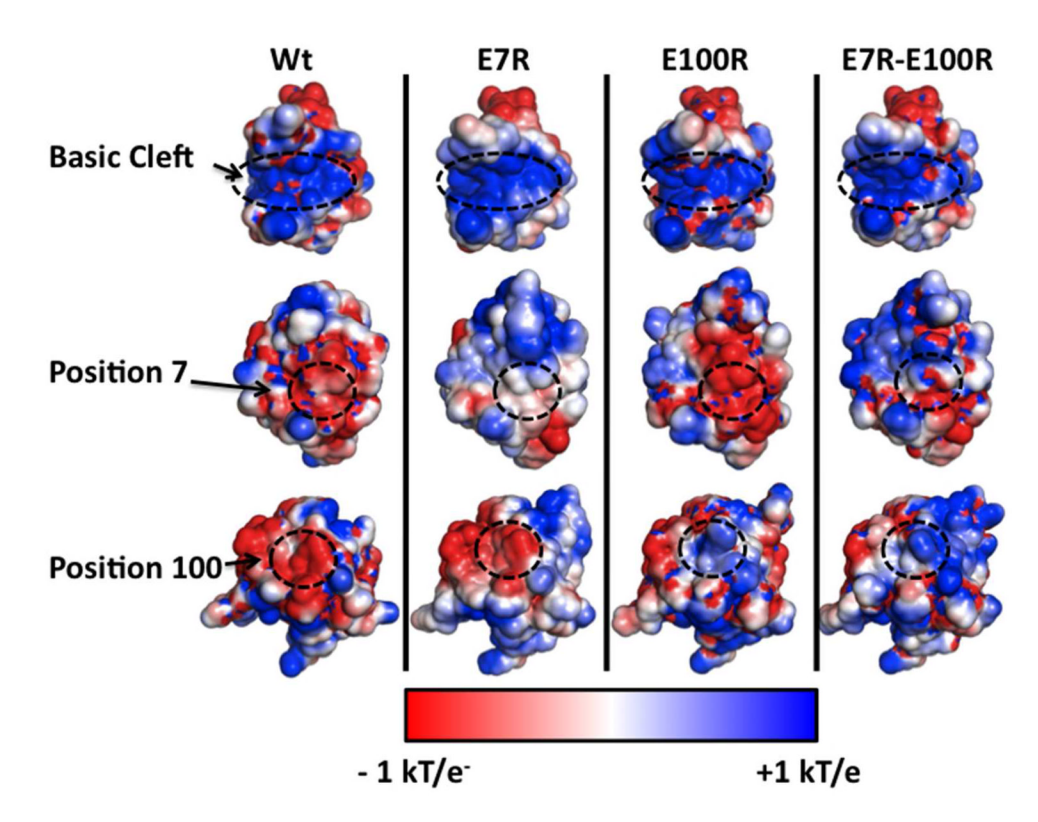


Figure 4. Electrostatic surface potentials of WT RPA70N and the E7R, E100R, and E7R, E100R mutants

Surface potentials calculated by the APBS software for (from left to right) WT, E7R, E100R and E7R, E100R. Dashed circles are drawn to highlight the basic cleft, residue 7, and residue 100.

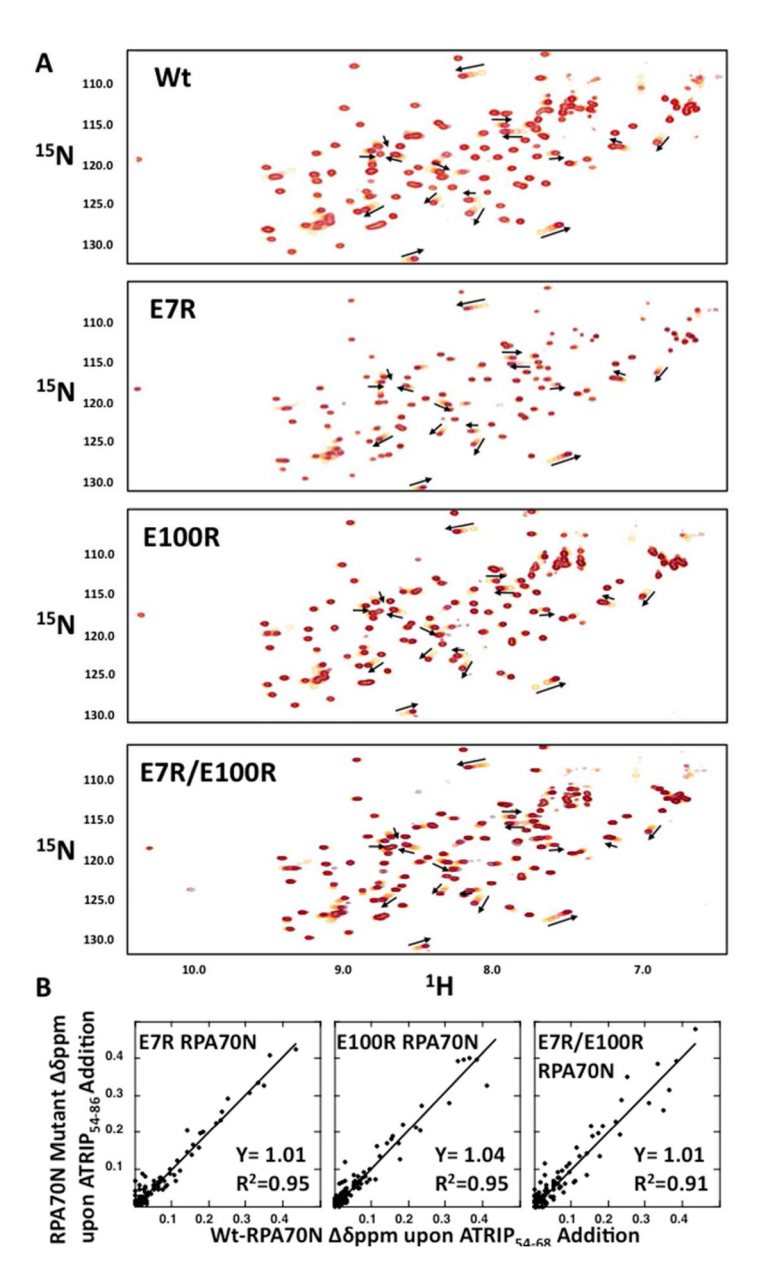


Figure 5. Comparison of NMR chemical shift perturbations induced by binding of ATRIP₅₄₋₆₈ in WT RPA70N and the E7R, E100R, and E7R, E100 mutants

A) NMR titration of WT RPA70N and the E7R, E100R, and E7R, E100 mutants with ATRIP54-68. Overlay of 15 N- 1 H HSQC spectra of WT RPA70N and the E7R, E100R, and E7R, E100R mutants as ATRIP54-68 is titrated into the sample. Base 15 N- 1 H crosspeaks transition from yellow to dark red upon ATRIP₅₄₋₆₈ saturation. Arrows indicate the starting and ending points for select residues exhibiting chemical shift perturbations as ATRIP₅₄₋₆₈ is added. B) Correlation plots comparing the chemical shifts in complexes with ATRIP₅₄₋₆₈ for mutant (y-axis) and WT RPA70N (x-axis).

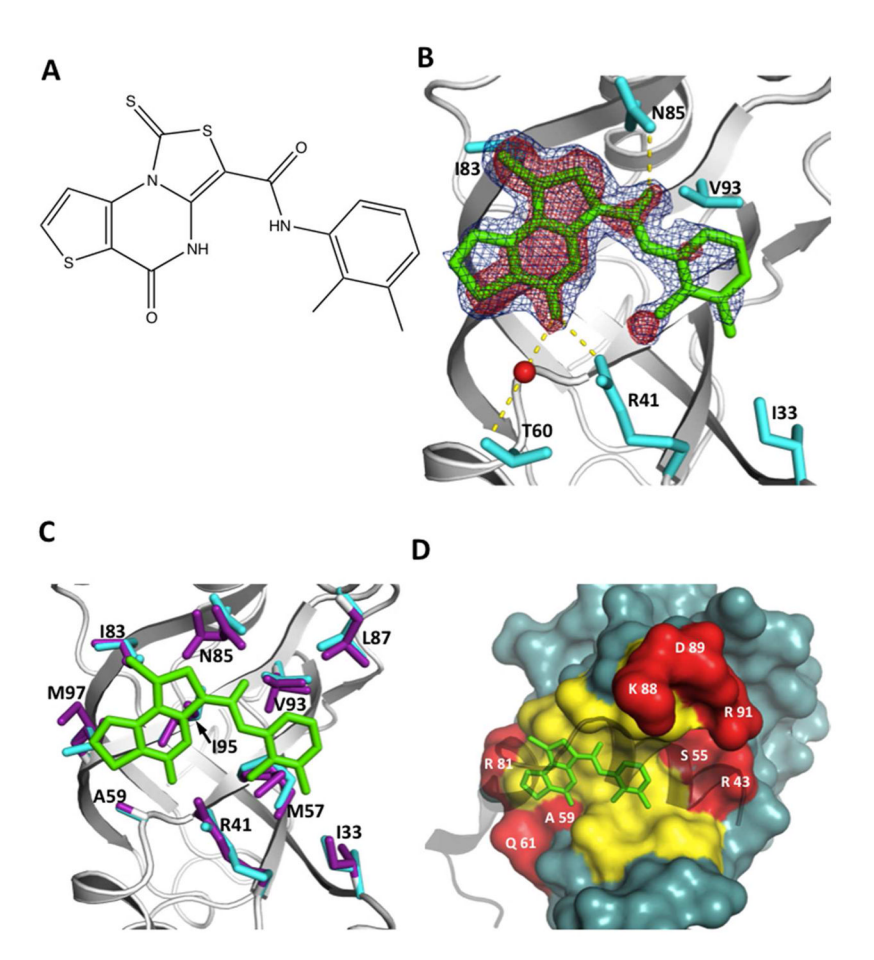
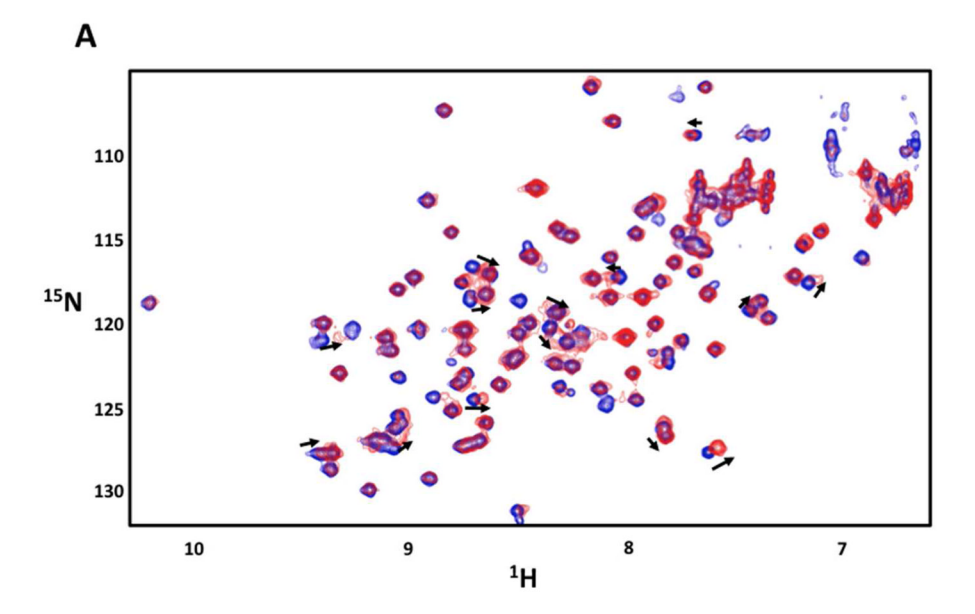


Figure 6. Structure of RPA70N E7R in complex with VU079104

A) Chemical structure of VU079104. B) Structure of RPA70N E7R colored to highlight side chains (cyan) within 3.5 Å of VU079104 (green), a crystallographic water (red sphere), and hydrogen bonding interactions to VU079104 (yellow dashes). VU079104 2F_o-F_c and F_o-F_c electron density maps are displayed contoured at 1 and 3 in blue and red mesh respectively. C) Changes in E7R side chains induced by binding of the ligand. The overlay shows the positioning of side chains within 3.5 Å of VU079104 (green) for E7R (purple sticks) and the E7R-VU079104 complex (cyan). D) Superposition of VU079104 (sticks) from the structure of the complex onto the surface of the structure of the RPA70N-p53 complex (PDB ID: 2B3G). Solvent exposed surface residues within 4 Å of VU079104 and p53 peptide (black) are colored yellow and red, respectively.



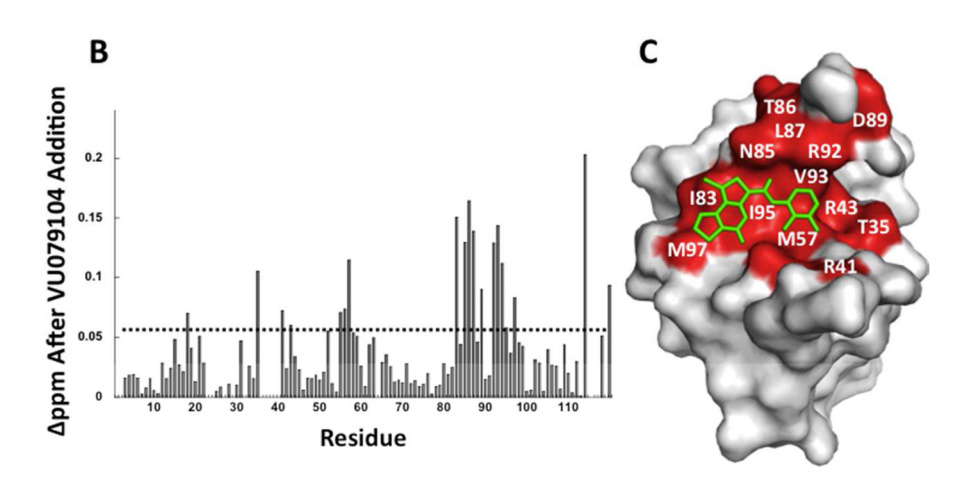


Figure 7. ¹⁵N-¹H chemical shift changes in WT-RPA70N induced by binding of VU079104 A) Overlaid ¹⁵N-¹H spectra of WT-RPA70N (blue) and VU079104 saturated WT-RPA70N (red), arrows indicated the direction of movement of select ¹⁵N-¹H cross peaks. B) Quantified chemical shift perturbations induced upon binding of VU079104 to WT RPA70N. C) Locations of significantly perturbed Wt-RPA70N residues (red) upon VU079104 addition mapped upon the structure of E7R RPA70N in complex with VU079014 (green sticks).

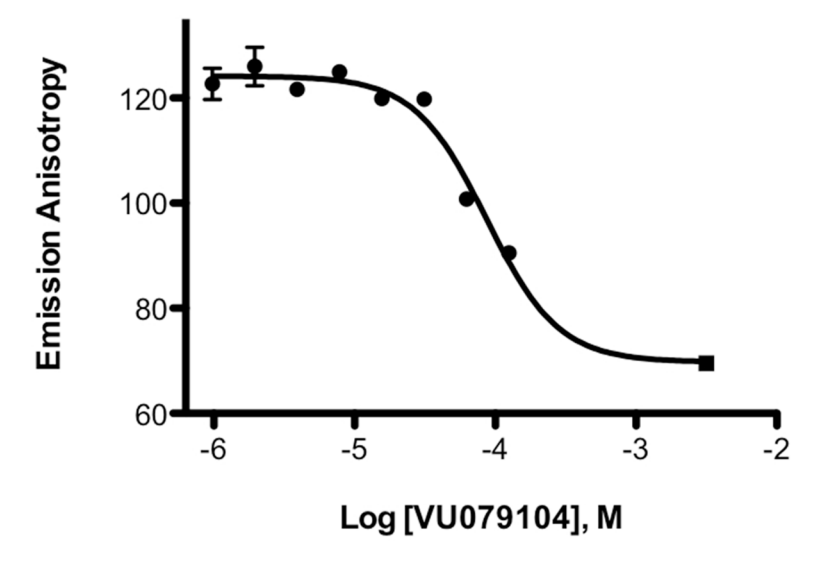


Figure 8. Fluorescence polarization anisotropy assay of the displacement of ATRIP $_{54\text{-}68}$ from RPA70N by VU079104

Concentration—response curve used for determination of the K_d for binding of VU079104 to WT-RPA70N. The error bars represent standard deviations of two independent experiments, each performed in duplicate. The data point represented by the square symbol corresponds to the anisotropy value recorded for ATRIP₅₄₋₆₈ in the absence of RPA70N.

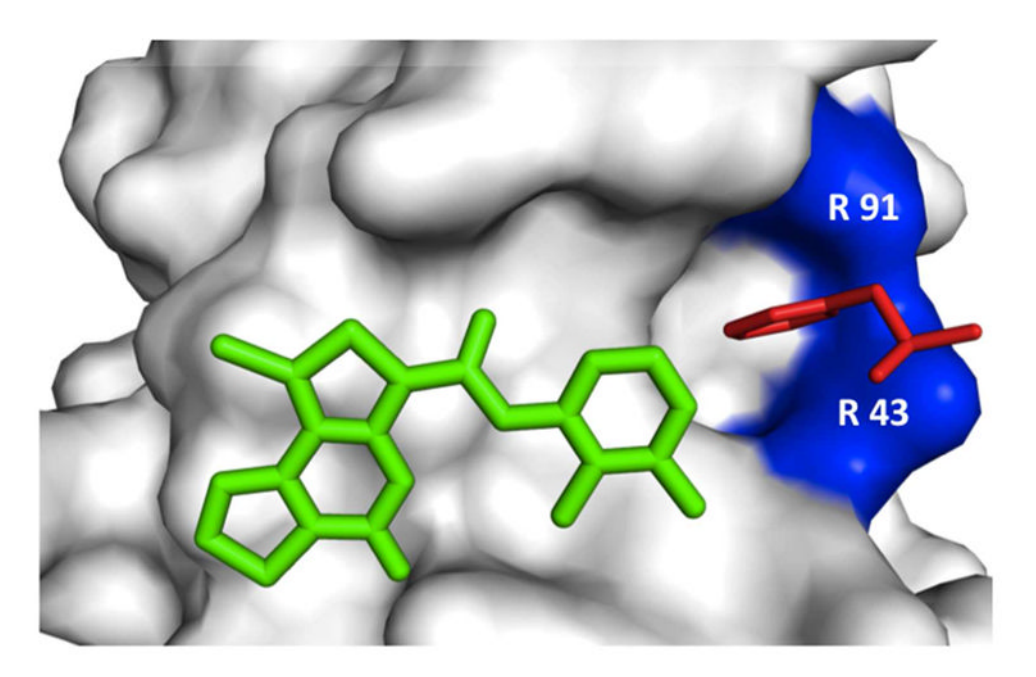


Figure 9. Comparative structural analysis suggests targeting of the S55 pocket to increase the affinity of the VU079104 framework for RPA70N $\,$

Superposition of VU079104 onto the surface of the structure of the RPA70N-p53 peptide fusion (PDBID: 2B3G) showing the close proximity of VU079104 to the hydrophobic pocket into which the F54 ring of p53 is inserted (red), and a basic patch on RPA70N created by residues R43 and R91 (blue).

Table 1

Model statistics

	E7R RPA70N	E100R	E7R, E100R	E7R RPA70N-Compound
PDB ID	4IPC	RPA70N 4IPD	RPA70N 4IPG	4IPH
Data Collection				
Wavelength (Å)	0.97857	0.97857	0.97857	0.97857
Space group	$P2_12_12_1$	P2 ₁ 2 ₁ 2 ₁	P2 ₁ 2 ₁ 2 ₁	P2 ₁ 2 ₁ 2 ₁
Cell dimensions				
a, b, c (Å)	38.54, 53.72,	39.43,	38.49, 53.79, 54.38	38.27, 54.27, 54.33
a, b, g (°)	90, 90, 90	90, 90, 90	90, 90, 90	90, 90, 90
Resolution (Å)	50-1.22	50-1.51	50–1.58	50–1.94
<i>R</i> _{sym} (%)	5.7	9.9	6.5	10.6
I/dI	15.37 (2.55)	40.38	18.30 (2.54)	14.33 (2.91)
Completeness (%)	99.72 (99.97)	99.24	99.92 (100.00)	98.31 (97.70)
Redundancy	5.9 (5.9)	8.4 (8.0)	5.9 (5.9)	5.7 (5.7)
Refinement				
Resolution	31.44 (1.22)	36.05 (1.51)	24.27 (1.58)	31.28 (1.94)
No. reflections	202226	139424	94894	49814
R_{work} (%)	14.74 (20.03)	13.76	16.34 (19.53)	19.63 (22.62)
R _{free} (%)	17.55 (25.35)	16.59	20.07 (23.86)	27.37 (31.26)
No. atoms	2322	2288	2210	1113
Protein	1049	1030	987	955
Ligand	-	-	-	50
Water	123	156	148	108
B-factors (Ų)				-
Average	20.2	10.7	19.8	24.7
Protein	18.8	9	17.8	21.9
Water	31.5	22.5	33.2	34.3
RMSD				
Bond lengths (Å)	0.009	0.007	0.018	0.011
Bond angles (°)	1.37	1.3	1.8	1.26
Ramachandran				
Most favored (%) plot	96	97	98	98
Allowed (%)	3.3	3	2	2
Disallowed (%)	0.7	0	0	0

Values in parentheses refer to the highest resolution shell

Table 2

Affinity of RPA70N for ATRIP $_{54-68}$

RPA70N Construct	K _d (µM)
Wt	5.61 ±0.84
E7R	5.01 ±0.30
E100R	7.67 ±0.32
E7R-E100R	3.64 ±0.54